Tellus
SERIES B
CHEMICAL
AND PHYSICAL
METEOROLOGY
PUBLISHED BY THE INTERNATIONAL METEOROLOGICAL INSTITUTE IN STOCKHOLM

Tellus (2010), 62B, 209–227
Printed in Singapore. All rights reserved

TELLUS

Study of CO surface pollution in Europe based on observations and nested-grid applications of GEOS-CHEM global chemical transport model

By ANNA P. PROTONOTARIOU[1], MARIA TOMBROU[1], CHRISTOS GIANNAKOPOULOS[2]*, EFFIE KOSTOPOULOU[2] and PHILIPPE LE SAGER[3], [1]*National and Kapodistrian University of Athens, Department of Physics, Division of Environmental Physics and Meteorology, Build. Phys. V, University Campus, Zografou, 157 84, Athens, Greece*; [2]*Institute for Environmental Research and Sustainable Development, National Observatory of Athens, V. Pavlou and Metaxa Str., GR-15236 Palaia Pendeli, Athens, Greece*; [3]*Division of Engineering and Applied Sciences and Department of Earth and Planetary Sciences, Harvard University, Cambridge, MA 02138, USA/Royal Netherlands Meteorological Institute, De Bilt, The Netherlands*

(Manuscript received 29 July 2009; in final form 17 May 2010)

ABSTRACT

Carbon monoxide (CO) is studied over Europe for 2001 using measurements from 31 rural-background stations and the nested-grid application of the global CTM GEOS-CHEM. The model reveals lowest (highest) biases in warm (cold) periods, tracking observations in most cases more closely than the global model. The role of CO production and destruction processes and the atmospheric conditions are investigated. A rotated Principal Component Analysis is applied to all stations, based on daily CO modelled concentrations in 2001, yielding three principal components (PCs) with stations of common characteristics. CO concentrations are studied for these groups in relation to the circulation patterns prevailing over Europe in 2001, at mean sea level and 850 hPa. The nested-grid model improves results in comparison to those calculated by the global model by up to ∼22% for first principal component subregion, where emissions are high and elevation is low. Improvement reaches ∼17 and ∼7%, respectively, for second and third principal component subregions, where emissions are lower and altitudes are higher. Better performance is achieved for patterns associated with westerly flow, whereas poor skills are revealed during stagnant conditions. During pollution events, the nesting model's ability in capturing CO surface concentrations improves by up to ∼40% in comparison to the global simulation.

1. Introduction

Carbon monoxide (CO) plays a significant role in the troposphere, converting hydroxyl radical (OH) to hydroperoxyl radical (HO_2). The low OH concentrations are associated with decreases in the oxidation of CH_4, leading to higher levels of this greenhouse gas in the atmosphere (e.g. Crutzen and Zimmermann, 1991; Jacob, 1999). Furthermore, the increased HO_2 oxidizes NO to NO_2, enhancing concentrations of ozone, which also acts as greenhouse gas. Therefore, while CO is not considered a direct greenhouse gas, it has the potential to contribute to global warming (Daniel and Solomon, 1998). Moreover, exposure to high CO levels may affect human health (e.g. Raub, 1999; Raub et al., 2000; Min et al., 2009). The estimation of past and present CO concentrations in the atmospheric surface layer over the European territory is crucial for assessing the effectiveness of emission control policies. Air-quality data, collected at background air monitoring stations in several European locations, provides information on CO distribution, while numerical modelling assists to identify and interpret the factors controlling CO pollution.

Nesting procedure, considering high-resolution grids, was first applied in a coarse-resolution global atmospheric chemical transport model (CTM) to simulate advective transport (Berkvens et al., 1999). More recently, full-nesting capabilities have been developed in global CTMs (Bergamaschi et al., 2007; Kaminski et al., 2008). The nested-grid application of GEOS-CHEM was first developed for Asia (Wang et al., 2004a) using boundary conditions from the global simulation. It was found that a more efficient ventilation of the lower atmosphere was simulated by the high-resolution model, reflecting intense upward motions over localized regions, which were not resolved

*Corresponding author.
e-mail: cgiannak@meteo.noa.gr
DOI: 10.1111/j.1600-0889.2010.00462.x

in the coarse-resolution simulation. Furthermore, the nested-grid model simulated realistically the frontal lifting processes and the differences across the boundary, separating more clearly the regions of cyclonic and anticyclonic flow than the low-resolution model. The nested-grid configuration of GEOS-CHEM has further been applied for Asia (Wang et al., 2004b, 2009b; Chen et al., 2009) and North America (Fiore et al., 2005; Li et al., 2005; Park et al., 2006; Wang et al., 2009a); however, a nested-grid version of this model has not been applied for Europe so far.

Carbon monoxide has relatively simple chemistry and chemical lifetime of 30–90 d in the troposphere, with typical rural background values being below 200 ppbv (Parrish et al., 1991, 1994; Seinfeld and Pandis, 2006). Measurements (Novelli et al., 1992, 1998a,b; Derwent et al., 1998) and global modelling applications (Kanakidou et al., 1999; Kanakidou and Crutzen, 1999) have shown that CO surface distribution in the northern hemisphere reflects mainly direct emissions, photochemical production by CH_4 and NMVOCs, destruction by OH radical (IPCC, 2001, Table 1), as well as advection and convection away from the source regions.

Carbon monoxide concentrations, derived from rural background stations of an extended air monitoring network, together with results calculated by the nested-grid configuration of the global CTM GEOS-CHEM, are studied in Europe for the year 2001. A specific objective of this study is to investigate the factors controlling the nested-grid model's performance in comparison to the global model. A rotated Principal Component Analysis (PCA) is applied to daily CO concentrations, calculated by both model configurations for 2001, in order to classify all stations in groups with common characteristics. Common features and dissimilarities between the two simulations, as well as statistical analysis based on measurements and model calculations, are examined in relation to anthropogenic emissions that dominate at surface layer in Europe (Jacob, 1999; Kanakidou and Crutzen, 1999; Pfister et al., 2004), chemistry, synoptic circulation patterns, transport and mixing processes. Additionally, two case studies of high CO pollution events in Europe are studied, associated with transport of anthropogenic or biomass burning origin pollutants. The synoptic conditions, as well as other meteorological parameters related to these events, are further discussed.

Table 1. Global annual sources and sinks of CO in the atmosphere [Tg (CO) yr^{-1}] considered in GEOS-CHEM model

CO sources and sinks	IPCC	GEOS-CHEM
Total sources [Tg (CO) yr^{-1}]	1800–2780	2256
Fossil fuels/industry[a]	300–650	402
Biofuels[a]	60–160	173
Biomass burning[a]	300–700	491
Biogenic	200–600	366
CH_4 oxidation	400–1000	824[b]
Oceans	20–200	–
Total sinks [Tg (CO) yr^{-1}]	2100–3000	2100–2655
Oxidation by OH	1500–2700	2100–2655
Stratospheric diffusion	∼100	–
Soil uptake	250–640	–

Note: Intergovernmental Panel on Climate Change (IPCC, 2001) estimates are also presented.
[a]Includes NMHCs oxidation.
[b]Mean value calculated for the global model simulation (Duncan et al., 2007).

2. The GEOS-CHEM chemical transport model

GEOS-CHEM is a three-dimensional global atmospheric CTM, developed by the Atmospheric Chemistry Modeling Group of Harvard University (http://acmg.seas.harvard.edu/) and several research groups worldwide use it for various studies in the troposphere. The first model evaluation (Bey et al., 2001) showed that CO concentrations are underestimated by up to 50 ppbv, indicating a combination of excessive OH concentrations and underestimated CO emissions, particularly those of the biogenic and biofuel NMHCs. In order to improve the model's performance, several modifications have been introduced. For example, a modified chemical mechanism based on Ravishankara et al. (2002) has been considered, which decreased the global mean OH concentration by 10–15%. Moreover, updated emission inventories have been included in the model (Jacob et al., 2002; Duncan et al., 2003, 2007).

Several comparisons of the simulated CO concentrations with observations have demonstrated a quite good representation of rural CO concentrations in the troposphere by GEOS-CHEM on global scale (e.g. Heald et al., 2003; Jaeglé et al., 2003; Duncan et al., 2007). Nevertheless, rural CO levels over Europe are still fairly biased (Duncan and Bey, 2004; Auvray and Bey, 2005), revealing the need for further improvements on the model over this region.

The ozone–NO_x–hydrocarbon–sulphur chemistry mechanism coupled to aerosol chemistry (Martin et al., 2003; Park et al., 2003, 2004) is considered in the present model's version (v7-01-02), described by 41 tracers, more than 80 chemical species and 300 reactions. Stratosphere–troposphere exchange of ozone is simulated by the Synoz scheme (McLinden et al., 2000), considering a global cross-tropopause flux of 475 Tg (O_3) per year. Advection is calculated with a flux-form semi-Langrangian method (Lin and Rood, 1996). Moist convection is computed using convective, entrainment and detrainment mass fluxes, assimilated by the Goddard Earth Observing System (GEOS) of NASA Global Modelling and Assimilation Office (GMAO, http://gmao.gsfc.nasa.gov) (Allen et al., 1996a,b). Rapid and complete vertical mixing is assumed within the GEOS-diagnosed planetary boundary layer (PBL).

The base anthropogenic CO emission inventory included in the model is described by Wang et al. (1998). A year-to-year variability is taken into account, by scaling the emissions with specific factors (Bey et al., 2001). The model's inventory also includes fossil fuel emissions from the Global Emission Inventory Activity (GEIA) (Benkovitz et al., 1996), biofuel emissions (Yevich and Logan, 2003), non-methane hydrocarbon emissions (Piccot et al., 1992) and natural sources from biosphere, such as oceans, volcanic activity and lightning (Price and Rind, 1992). Biomass burning emissions are based on a climatological inventory (Wang et al., 1998), prescribed specifically to 2001 by using a combination of products from Total Ozone Mapping Spectrometer (TOMS) Aerosol Index (AI) and Along Track Scanning Radiometer (ATSR) World Fire Atlas (Duncan et al., 2003). Global sources and sinks of carbon monoxide considered in GEOS-CHEM on an annual basis, as well as those reported by the Intergovernmental Panel on Climate Change (IPCC, 2001), are summarized in Table 1. With respect to the European domain, fossil fuel and biofuel emissions contribute, respectively, 60.9 Tg (CO) and 11.2 Tg (CO) to the annual European CO budget. Contribution of the biogenic and biomass burning emissions accounts, respectively, for 2.4 Tg (CO) and 1.7 Tg (CO) every year. Oxidation by hydroxyl radicals is the only sink of carbon monoxide considered in GEOS-CHEM, as it represents globally 90–95% of total CO destruction (Logan et al., 1981).

3. Methodology

To meet the aims of this study, two distinct configurations of GEOS-CHEM are used: (a) the one-way nested-grid model over Europe and (b) the global model (without nesting). The terrain-following, sigma coordinate system is used in both model configurations, with 30 vertical levels up to 0.01 hPa and an average of nine layers to define the boundary layer below 2 km. The GEOS-3 assimilated meteorological data for 2001 (available by the GEOS/GMAO) and the emission inventories are provided in horizontal grid-resolutions of $1^\circ \times 1^\circ$ and $4^\circ \times 5^\circ$ for the nested-grid and the global model configurations, respectively.

In order to apply the nested-grid simulation (S_2) of GEOS-CHEM over Europe, a 2-yr (January 2000 to December 2001) full-chemistry simulation of the global model (S_1) is performed first. Hourly boundary conditions are saved around the nested domain, which includes Europe and parts of neighbouring countries in Africa, Middle East and Asia (20°W–45°E, 22°N–74°N, Fig. 1), only during the second simulation year, allowing for 1-yr model's spin up. These boundary conditions are implemented around the European domain when the nested-grid simulation is performed.

Due to the applied advection algorithm (Lin and Rood, 1996), a buffer zone of four $1^\circ \times 1^\circ$ grid-cells is considered (bounded by the two black rectangulars, Fig. 1), in order to separate the nested domain from the parent global domain. The concentrations in the fine grids in this zone are taken from the coarse-resolution simulation through an area-weighting, grid-filling procedure (Wang et al., 2004a). Moreover, the transport and the convective time-steps, which are set to 30 min in S_1, are reduced to 10 min for the nested-grid simulation, resulting in a far more efficient treatment of advection and convection processes in S_2.

Differences over the European nest between the surface geopotential heights considered in the global (bottom-left plot,

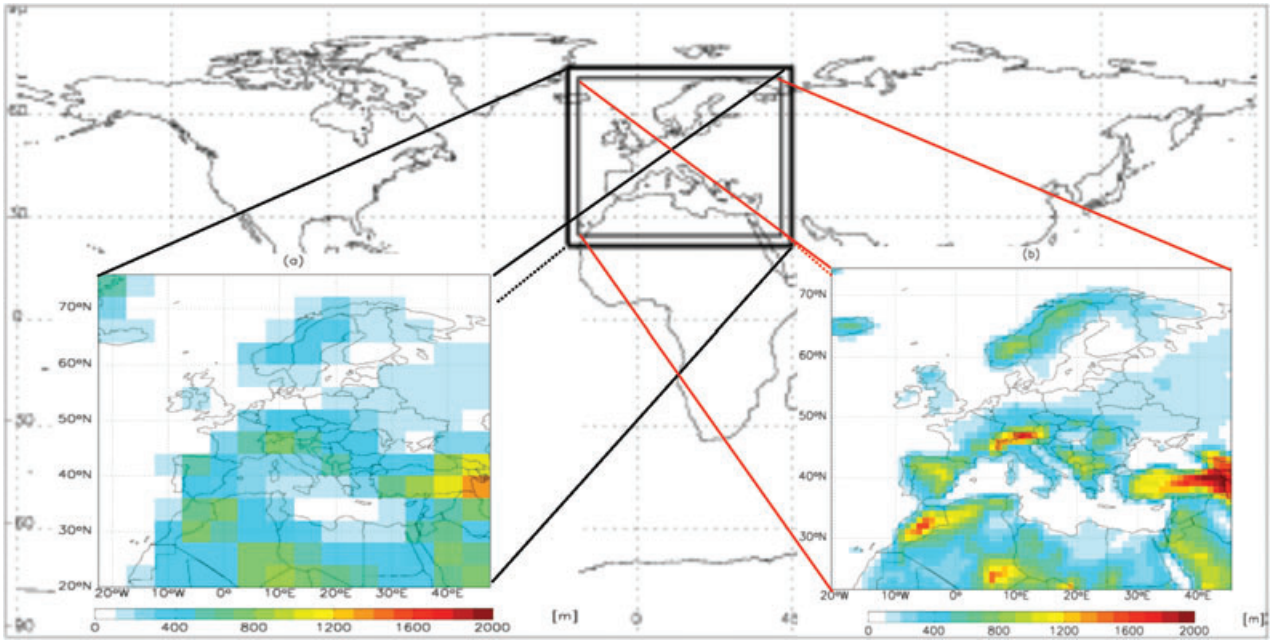

Fig. 1. Global and European (nested) modelling domains. The surface geopotential heights (in meters) are also shown over the nested domain (bottom-right plot for nested-grid model configuration, bottom-left plot for the global model).

Fig. 1) and the nested (bottom-right) domains reflect differences in the topography representation of the two model configurations due to their grid-resolutions. In particular, S_2 has proved to be more successful in representing the various topographic features, such as coastlines, water surfaces (e.g. the Mediterranean Sea and the Black Sea) and mountain ranges (e.g. the Alpine region), in comparison to the coarse depiction of the geophysical characteristics by S_1. This is especially important since topographic features can significantly impact transport and mixing, particularly over complex terrains. Indeed, as will be shown in Section 4.2, the altitude variations, in conjunction with the prevailing synoptic conditions, strongly affect the horizontal and vertical motions. On the other hand, the behaviour of the advection and convection processes is simple at flat terrains; convergence (divergence) of air masses at the surface takes place under low (high) pressure systems, with the air then lifting (sinking) through convection.

The spatial distribution of the anthropogenic CO emissions (Fig. 2) reveals that the major sources locate between the western and central mid-latitude Europe, which is the most heavily industrialized and densely populated part of the continent. Although the general pattern of these inventories is similar in the two model configurations, emissions are more homogenously distributed in the $4^\circ \times 5^\circ$ grids (Fig. 2a). On the other hand, greater emission variability is observed in the $1^\circ \times 1^\circ$ grids (Fig. 2b), favouring, as will be discussed later, this model configuration's ability to predict more accurate results.

In order to compare model calculations with observed time series (in Coordinated Universal Time, UTC), modelled concentrations are generated by sampling CO at the grid containing each sampling site. Observations from rural background stations, available from the public Air Quality Database (Airbase) of the European Environmental Agency (http://www.eea.europa.eu/data-and-maps/data/airbase-the-european-air-quality-database-1), are used in this study. This database includes sites close to or remote from anthropogenic sources, close to coast or inland and sites at high or low altitudes. During 2001, CO measurements from 43 European stations were available; however, data from 31 stations are used in this study, as more than 25% of the measurements are missing at the remaining stations. The examined stations are located in Austria, France, Germany, Italy, Poland, Switzerland, and the Netherlands (Fig. 3, Table 2). These stations are classified in groups, based on daily CO modelled concentrations in 2001 calculated by the nested-grid and the global models, by applying a rotated PCA (Wilks, 1995). Then, CO concentrations are studied for each principal component (PC) group in relation to the circulation patterns prevailing over Europe at the mean sea level (MSL) and at the geopotential level of the 850 hPa, the emission density and the altitude. Furthermore, CO is examined at one rural Greek station (Fig. 3), where measurements were available by the Mediterranean Intensive Oxidant Study (MINOS, Lelieveld et al., 2002a).

4. Results and discussion

4.1 Model results and performance

The spatial distribution of the mean monthly surface CO concentrations over Europe simulated by S_2 (Appendix S1 in Supporting Information) shows a strong latitudinal surface gradient, extending from the United Kingdom to eastern Europe, related to the distribution of anthropogenic CO sources (Fig. 2b). The highest mean monthly levels (up to 520 ppbv) are observed in winter (Appendix S1), partially due to the slow removal processes of CO by the low levels of OH during this season (5×10^2–2.5×10^6 molec cm^{-3}), resulting in a CO lifetime

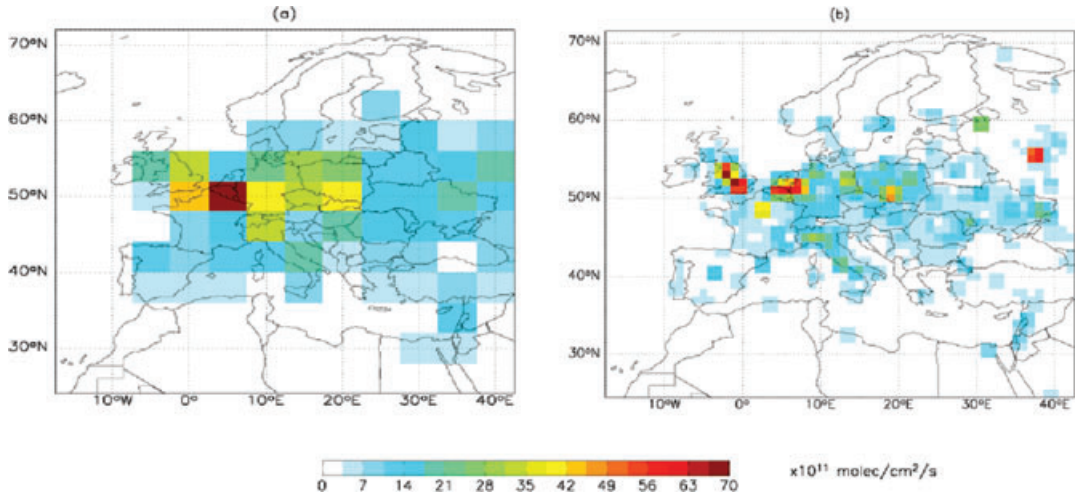

Fig. 2. Anthropogenic surface CO emissions in Europe considered by (a) the global model and (b) the nested-grid model.

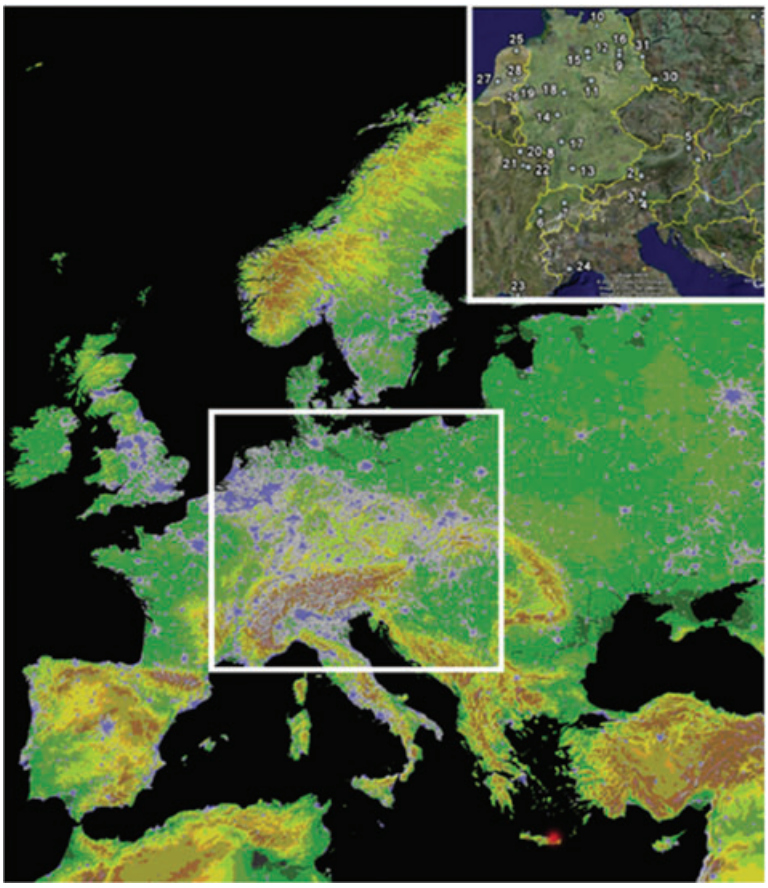

Fig. 3. Location of the 31 rural background stations available from the European Environmental Agency database considered in this study (high-resolution topography image source: ftp://ftp.ngdc.noaa.gov/GLOBE-DEM/pictures/). Upper-right rectangle zooms in at each station location, numbered according to the index (a/a) in Table 2. The rural background station of Finokalia, in Greece, is also shown with a red dot.

of 1–2 months. Additionally, CO tends to accumulate close to its sources in winter, forced by shallow mixing heights extending up to ∼400 m in the model, particularly over the highly polluted areas, in agreement with experimental values (Emeis and Schafer, 2006). On the other hand, lower CO concentrations (up to 300 ppbv) are present in summer (Appendix S1), attributed in part to the deep boundary layer mixing heights in this season (700–2000 m) that favour pollutants' dispersion. Moreover, CO levels are further decreased through its quick oxidization by the high summer OH concentrations (13×10^4–5×10^6 molec cm^{-3}) that results to a much shorter CO lifetime (weeks-to-month). High levels of OH are particularly evident along the coasts of southern Europe and over the Mediterranean in summer (Appendix S1), due to intense solar ultraviolet (UV) radiation flux, enhanced levels of local O_3 mixing ratios and high water vapour concentrations during this season. At less polluted areas of Europe, such as the Mediterranean basin, increased CO levels attributable mainly to European sources can be found, particularly under the influence of specific synoptic patterns (Kallos et al., 2007; Kostopoulou and Jones, 2007), and especially during warm periods (e.g. Lelieveld et al., 2002a). Nevertheless, CO concentrations at these areas remain lower in comparison to the continental and/or winter levels and are strongly controlled by the seasonal cycle of OH and the enhanced vertical mixing.

The comparison between spatial CO surface concentration distributions in the two simulations reveals that S_2 produces higher CO levels up to ∼65% in winter (30% in summer) than S_1 (Appendix S1), mainly close to high-polluted regions in western Europe at mid-latitudes. On the other hand, S_1 produces higher CO levels up to ∼30% in winter (25% in summer) mainly in areas far from large anthropogenic sources (e.g. eastern Europe and the Mediterranean region). These differences between the two models' calculations are attributed partially to the differences between the emission densities in the two inventories (Figs 2a and b), with CO emissions in the coarse grids of S_1 being dispersed over a larger area. Discrepancies are more pronounced near the coast, as the coarse grids include a large fraction of sea area. Moreover, differences in CO concentrations calculated by the two model's configurations are also related to the OH values. Differences in OH concentrations in the two models have a particularly variable pattern (Appendix S1), as the OH chemical balance is strongly controlled by its source and sink gases (Jacob, 1999; Lelieveld et al., 2002b, 2004). Therefore, these discrepancies in modelled OH concentrations are related to differences in NO_x, CO and other hydrocarbons emissions and O_3

Table 2. Alphabetical list of the stations in Europe considered in this study

a/a	Station ID	Station name	Longitude (deg)	Latitude (deg)	Altitude (m)	CO [$\times 10^{-6}$ Tg(CO) yr^{-1} km^{-2}]	
						S_1	S_2
1	AT0002R	Illmitz	16.766	47.769	117	4.1	8.6
2	AT0004R	St. Koloman Kleinhorn	13.233	47.651	1005	4.1	2.7
3	AT0005R	Vorhegg bei Kötschach-Mauthen	12.972	46.680	1020	4.1	2.4
4	AT0141A	Obervellach Schulzentrum	13.196	46.936	686	4.1	2.4
5	AT0159A	Langenzersdorf	16.361	48.303	160	12.0	6.9
6	CH0002R	Payerne	6.946	46.801	430	6.8	7.9
7	CH0005R	Rigi	8.465	47.056	1030	13.0	7.5
8	DE0502A	Eggenstein	8.405	49.083	110	14.5	8.7
9	DE0754A	Grunewald	13.228	52.474	50	10.0	21.3
10	DE1023A	Gülzow	12.067	53.821	17	4.0	3.2
11	DE1082A	Harzgerode	11.099	51.659	385	14.5	7.0
12	DE1128A	Salzwedel	11.174	52.857	20	4.0	7.9
13	DE1140A	Schwïbische Alb	9.209	48.346	799	14.5	10.1
14	DE1172A	Linden/Leihgestern	8.687	50.534	173	14.5	10.7
15	DE1197A	Zartau/Waldstation	11.175	52.594	100	4.0	7.9
16	DE1226A	Frohnau, Funkturm	13.293	52.654	50	10.0	16.8
17	DE1242A	Odenwald	8.755	49.455	520	14.5	10.4
18	DE1256A	Zierenberg	9.272	51.362	469	14.5	10.7
19	DE1303A	Borken-Gemen	6.876	51.863	45	25.7	36.0
20	FR0586A	Moyeuvre	6.052	49.260	230	25.7	4.8
21	FR1023A	Hotel Districal	6.181	48.686	200	25.7	4.8
22	FR1032A	Luneville	6.483	48.603	230	25.7	4.8
23	FR1104A	Port de Bouc EDF	4.986	43.431	25	4.5	6.1
24	IT1233A	Cengio	8.217	44.393	400	13.0	7.5
25	NL0009R	Kollumerwaard-Hooge Zuidwal	6.278	53.332	1	4.0	11.0
26	NL0223A	Biest Houtakker-Biestsestraat	5.149	51.519	15	25.7	25.3
27	NL0229A	Zegveld-Oude Meije	4.838	52.139	0	4.0	25.3
28	NL0247A	Loenen-Eerbeeksedijk	6.038	52.121	15	4.0	29.1
29	PL0014A	MzBelskIGPAN	20.792	51.837	180	14.9	14.3
30	PL0026A	DsJelw05	15.232	51.228	244	12.0	17.3
31	PL0030A	Urad	14.720	52.231	30	10.0	6.5

Notes: Station ID (second column) is declared by the country initial letters (AT, Austria; CH, Switzerland; DE, Germany; Fr, France; IT, Italy; NL, the Netherlands; PL, Poland) and an index number. The annual anthropogenic emission rate of CO [Tg (CO) yr^{-1} km^{-2}] at the grid-box of each station is also presented for the nested-grid (S_2) and the global (S_1) model simulations (7th/8th columns).

concentrations in the two model configurations. In particular, the lower OH concentrations close to major anthropogenic sources in Europe in the nested-grid configuration of GEOS-CHEM are attributed to denser anthropogenic CO, NO_x and hydrocarbons emissions in the fine grids, as well as to the reduced ozone concentrations (Appendix S1). Indeed, both these factors can lead to reduced radicals in the nested domain and consequently, less CO is removed by OH in urban and highly industrialized areas. On the other hand, chemistry balance at remote regions is strongly affected by transported pollution. Therefore, CO and OH concentrations at remote areas depend not only on the emissions and the background levels of their precursors, but on their transport as well.

CO is further examined at 31 European rural background stations (Fig. 4 and Appendix S2 in Supporting Information). It is worth noting that, although all stations considered in this study are characterized as rural-background, significantly enhanced concentrations are observed at some sites. For instance,

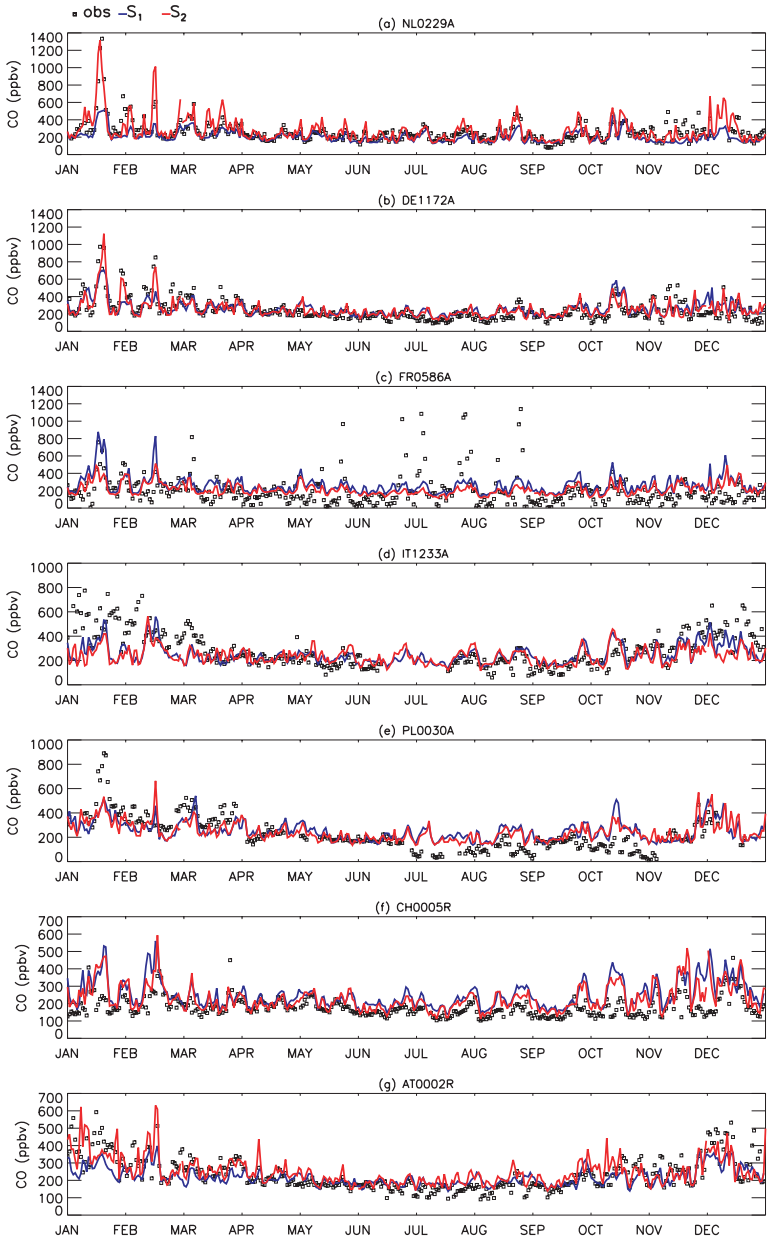

Fig. 4. Measured and modelled mean daily CO concentrations calculated by the nested-grid (S_2) and the global (S_1) simulations of GEOS-CHEM for seven stations in Europe during 2001.

mean daily CO concentrations in winter can reach levels that are usually observed at rural suburban or even urban regions (e.g. Figs 4a and b). On the other hand, surface CO levels remain low at some other stations throughout the year (e.g. Figs 4f and g). The factors controlling CO levels at the stations included in this study are examined in the next sections.

Table 3 summarizes the statistical parameters calculated by all measured and modelled pairs of mean monthly CO concentrations at all stations in 2001. The nested-grid model configuration captures the CO cycle reasonably well throughout the year ($R_{S2}{}^2 = 0.63$), similar to the global model. There is a small tendency to underestimate the average values of the observations (MO = 248.8 ppbv), as denoted by the mean bias ($MB_{S2} = -4.5$ ppbv). The magnitude of this underestimation is moderate, as attested by the mean error ($ME_{S2} = 76.7$ ppbv). Regarding the overall seasonal performance, S_2 shows lower biases from the observations in warm periods (median spring/summer $MB_{S2} = 3.7$ ppbv, median $ME_{S2} = 59.6$ ppbv) than in cold periods (median $MB_{S2} = -12.7$ ppbv, $ME_{S2} = 95.8$ ppbv). Model performance at each station is further studied individually, using monthly averages (Table 4). The higher correlation coefficient at all stations, as well as the lower mean biases and errors at most sites, indicates that the nested-grid model configuration is capable of reproducing CO concentrations in Europe more

Table 3. Statistical parameters of the observed and the calculated by the nested-grid (S_2) and the global (S_1) simulations of GEOS-CHEM mean monthly CO concentrations in Europe, on an annual and seasonal basis for 2001

Period	M_O (ppbv)	M_{ES} (ppbv)		S_d (ppbv)			*MB* (ppbv)		*ME* (ppbv)		R^2	
	Obs	S_1	S_2	Obs	S_1	S_2	S_1	S_2	S_1	S_2	S_1	S_2
Annual	248.8	244.4	244.2	111.6	72.2	75.6	−4.4	−4.5	78.9	76.7	0.58	0.63
Winter	316.6	301.4	303.3	125.1	74.0	77.0	−15.2	−13.2	108.2	105.7		
Spring	236.9	238.3	241.4	88.6	70.3	78.1	1.4	4.5	67.4	64.7		
Summer	197.2	203.9	200.1	76.3	56.5	58.6	6.7	2.8	55.6	54.5		
Autumn	246.0	237.6	233.8	119.3	37.2	30.8	−8.4	−12.1	87.2	85.9		

Note: Statistical parameters equations can be found in the Appendix S3 in Supporting Information. R^2 is calculated only for the whole year, as it is indicative of the annual cycle representation.

Table 4. As in Table 3, but individually for each station of Table 2 on an annual basis

a/a	Station	M_O (ppbv)	M_{ES} (ppbv)		S_d (ppbv)			*MB* (ppbv)		*ME* (ppbv)		R^2	
		Obs	S_1	S_2	Obs	S_1	S_2	S_1	S_2	S_1	S_2	S_1	S_2
1	AT0002R	234.3	219.8	250.2	73.9	33.3	52.7	−14.5	15.9	37.6	29.0	0.82	0.85
2	AT0004R	185.2	219.8	208.1	25.6	33.3	25.3	34.6	22.9	34.6	22.9	0.78	0.79
3	AT0005R	187.1	219.8	207.0	24.9	33.3	28.0	32.7	19.9	34.6	21.5	0.63	0.66
4	AT0141A	300.2	219.8	207.0	95.4	33.3	28.0	−80.4	−93.3	80.4	93.3	0.74	0.76
5	AT0159A	393.6	270.7	243.1	94.3	51.5	45.4	−122.9	−150.5	122.9	150.5	0.63	0.66
6	CH0002R	243.0	215.1	233.2	63.2	36.2	42.5	−27.9	−9.8	40.0	34.3	0.51	0.65
7	CH0005R	180.5	250.0	231.5	25.4	41.7	40.2	69.4	50.9	69.4	50.9	0.57	0.58
8	DE0502A	273.1	264.6	238.5	88.8	55.6	42.0	−8.4	−34.6	34.6	41.2	0.86	0.79
9	DE0754A	165.6	204.8	221. 0	43.6	44.7	64.3	39.2	55.4	41.6	55.4	0.73	0.74
10	DE1023A	227.6	231.5	215.8	62.6	55.1	53.5	3.9	−11.9	32.9	24.4	0.57	0.69
11	DE1082A	216.3	264.6	238.7	35.6	55.6	51.0	48.4	22.4	56.7	36.9	0.40	0.41
12	DE1128A	202.1	193.3	194.4	20.7	56.6	57.8	−8.8	−7.7	39.3	36.3	0.29	0.49
13	DE1140A	132.6	222.0	193.8	28.7	56.8	41.1	89.4	61.2	89.4	61.2	0.71	0.53
14	DE1172A	246.1	264.6	256.4	78.4	55.6	48.3	18.6	10.4	41.8	41.1	0.67	0.68
15	DE1197A	173.1	193.3	194.4	42.7	56.6	57.8	20.2	21.3	41.3	36.1	0.36	0.48
16	DE1226A	147.9	210.2	215.3	43.9	47.1	63.5	62.4	67.5	62.4	67.5	0.78	0.88
17	DE1242A	149.7	222.0	205.3	43.1	56.8	48.0	72.3	55.6	72.3	56.0	0.49	0.53
18	DE1256A	138.3	222.0	213.2	22.9	56.8	48.9	83.7	74.8	83.7	74.8	0.6	0.67
19	DE1303A	241.5	218.4	264.3	60.2	43.9	71.2	−23.1	22.8	31.5	44.5	0.66	0.53
20	FR0586A	201.1	262.0	216.8	70.6	42.0	33.2	60.9	15.8	87.2	61.8	0.10	0.10
21	FR1023A	487.8	252.4	212.5	116.6	28.8	31.3	−235.4	−275.3	235.4	275.3	0.30	0.30
22	FR1032A	470.1	262.0	216.8	92.0	42.0	33.2	−208.2	−253.3	208.2	253.3	0.60	0.82
23	FR1104A	385.2	199.0	239.2	67.8	20.9	43.1	−186.2	−146.0	186.2	146.0	0.10	0.10
24	IT1233A	306.3	259.6	245.2	125.7	39.1	24.2	−46.7	−61.1	82.7	94.8	0.57	0.61
25	NL0009R	218.7	208.7	237.9	45.8	33.8	58.0	−9.9	19.2	19.1	25.6	0.58	0.75
26	NL0223A	307.3	262.0	272.9	75.5	42.0	64.9	−45.4	−34.4	48.2	36.2	0.63	0.79
27	NL0229A	271.5	208.7	272.8	66.5	33.8	64.9	−62.8	1.3	62.8	26.3	0.84	0.90
28	NL0247A	265.1	208.7	290.5	73.5	33.8	70.8	−56.3	25.5	56.6	39.3	0.44	0.74
29	PL0014A	338.9	277.3	271.7	89.5	54.2	55.0	−61.6	−67.3	70.5	75.0	0.4	0.42
30	PL0026A	230.5	261.1	269.4	39.1	51.8	50.6	30.6	38.9	30.9	38.9	0.68	0.75
31	PL0030A	223.1	249.3	247.9	124.8	45.4	49.5	26.3	24.9	84.0	75.0	0.71	0.74

Table 5. Statistical parameters of the observed and the calculated by the nested-grid (S_2) and the global (S_1) simulations of GEOS-CHEM mean monthly CO concentrations at station Zegveld-Oude Meije (NL0229A) in the Netherlands on an annual and seasonal basis in 2001

NL0229A	M_O (ppbv)	M_{ES} (ppbv)		S_d (ppbv)			*MB* (ppbv)		*ME* (ppbv)		R^2	
	Obs	S_1	S_2	Obs	S_1	S_2	S_1	S_2	S_1	S_2	S_1	S_2
Annual	271.5	208.7	272.8	66.5	33.8	64.9	−62.8	1.3	62.8	26.3	0.84	0.9
Winter	340.2	231.7	347.6	88.3	31.7	47.8	−108.5	7.4	108.5	35.9		
Spring	262.8	223.6	285.0	41.8	31.7	65.0	−39.2	22.1	39.2	30.4		
Summer	236.7	185.7	228.9	17.6	9.5	13.5	−51.0	−7.8	51.0	7.8		
Autumn	246.2	193.9	230.2	34.5	30.9	25.6	−52.3	−16	52.3	31.1		

accurately than the global simulation. The good performance of the nesting model approach is particularly apparent for stations close to significant anthropogenic activity and/or close to the coast, as in these cases statistics in S_2 are significantly improved in comparison to those calculated for in S_1 (e.g. up to ∼23% for station NL0229A). Improvement is also evident for stations at high altitudes, with the statistical metrics in S_2 being lower by up to ∼10% than those in S_1 in Switzerland, Austria and Germany. The most unbiased performance is found at NL0229A; hence this site has been selected for further statistical analysis (Table 5). The strong correlation ($R_{S2}{}^2 = 0.90$) and the low deviation (<10%) highlight the nested-grid model benefits. The factors that favour the improvement on the nested-grid model's results in comparison to the global model are investigated in the next section.

Some sources of biases are detected in the nested-grid application of GEOS-CHEM. Among them, are those attributed to the fact that the CO anthropogenic emissions in the model do not vary through the seasons. However, such biases are not significant, as CO seasonal variations from fossil fuel combustion in the model deviate only by up to ∼8% from the annual means (Duncan and Bey, 2004). The corresponding high correlation coefficients (Tables 3–5) prove the good representation of the CO annual cycle by the model. Some other uncertainties in emissions can induce further model biases. In particular, although the biomass burning emissions, which are usually a large source of bias, are satisfactorily updated for 2001 (Duncan et al., 2003), their injection heights are not precisely defined. Additionally, model deviations can be also attributed to the full-mixing PBL scheme considered in the model, assuming that surface emissions and concentrations are distributed evenly within the mixing layer. This is a rational assumption when the PBL is extremely unstable, but it will overestimate vertical mixing when the PBL is modestly or weakly unstable, neutral or stable. The grid size in the nested-grid model, although of higher resolution, still limits modelling skills in simulating small-scale weather systems (in scales smaller than $1^\circ \times 1^\circ$ resolution, resulting occasionally in mismatches in the meteorological data representation), as well as emissions and model predictions (cell average) at station-scales (point value); hence the accuracy of the results is reduced. Finally, since CO production from oceans, CO removal through soils and CO stratospheric diffusion are not included in the model, further biases can be induced in the model calculations, but to a lesser degree, since they represent smaller source and sinks, respectively.

4.2 Sensitivity study

Differences between CO concentrations simulated by the nested-grid and the global models reflect differences in CO production and destruction processes in the two model configurations, as well as discrepancies in the factors that directly or indirectly impact these processes. In order to investigate the factors that favour the improvement on the nested-grid model's results in comparison to the global model, the sensitivity of the two model configurations to synoptic circulation patterns, CO anthropogenic emissions, transport and mixing processes is studied in this section.

First, a PCA is applied to both S_1 and S_2 data sets of daily CO modelled concentrations during 2001, in order to classify the 31 stations in groups. The PCA yields three PCs, which define the three subregions shown in Fig. 5, accounting for the suggested from the literature >80% of the total variance (Jolliffe, 1993). It is evident that this grouping provides clearer spatial distribution regarding the S_2 data set. Moreover, it is worth noting that the PCA results are associated with the geographical location of the stations, as well as with the emission intensity. The first principal component (PC1, explaining 33.7% of the total variance in the original data set) accumulates stations located in the northern and western part of the study region, close to the major anthropogenic sources. Therefore, the stations belonging in PC1 subregion should be affected to a large degree by emissions. In this group, the mean emission rate in S_2 is significantly higher (up to ∼50%) than that in S_1. This is explained by the fact that most of these stations are close to the coast and the coarse grids of S_1 include a large fraction of sea area. The second principal component (PC2, capturing 24.8% of the total variance) includes stations that are located in the southern part of the examined area, with their majority being remote from major sources. In this group, the mean value of the emissions

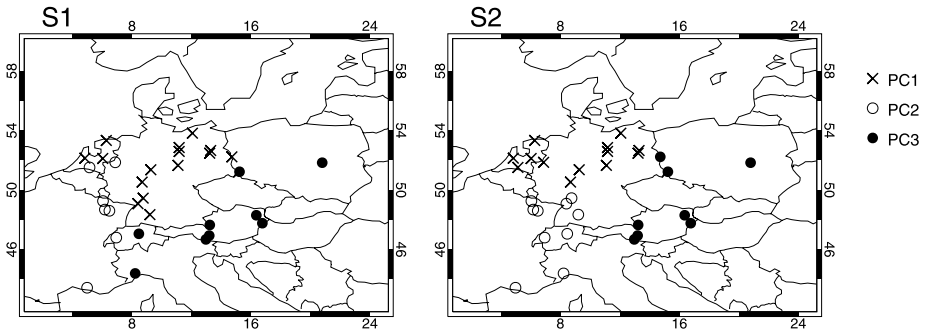

Fig. 5. Three principal components (PCs) in S_1 and S_2 data sets obtained from rotated Principal Component Analysis (PCA), defining three subregions: PC1 (x), PC2 (open circles) and PC3 (filled circles).

in S_2 corresponds to ∼1/3 of that considered in S_1 and to ∼1/2 of that in PC1 group. Moreover, it is worth noting that the real mean altitude of PC2 group is approximately 400 m, which is closer to the mean altitude considered by S_2 (∼500 m) than by S_1 (∼270 m) and much higher from the one in PC1 group (∼120 m). Therefore, model results for PC2 subregion are expected to be significantly influenced by the effects of topography. Regarding the third principal component (PC3, accounting for 22.6% of the total variance), the stations are located in the eastern part of the examined area, with lower background emissions in comparison to the other two groups and at similar mean altitudes with PC2 subregion.

Atmospheric circulation plays an important role in air-quality studies, particularly for CO (e.g. Liu et al., 2006). To evaluate the performance of S_2 compared to S_1, the relationship between their modelled CO concentrations is examined for each PC group, in relation to the 13 circulation patterns at MSL over Europe, based on the classification developed by Kostopoulou and Jones (2007). In addition, an upper level (850 hPa) classification is also used, considering 9 circulation modes (Kostopoulou, 2003).

The 13 circulation types (CTs) at MSL are used to classify the daily weather conditions during 2001. Composites of these types are presented at Appendix S4 in Supporting Information. The first five patterns feature a major centre of high pressure. In the first circulation type (CT1), the anticyclone is located in northwestern Europe and the centre is observed over the Benelux Region. In CT2, the Siberian High is the main centre, which dominates over eastern Europe, spreads over a large part of Scandinavia and expands to the south reaching the Mediterranean. This circulation comprises a prevailing feature in the winter season. The next three patterns (CT3, CT4 and CT5) feature anticyclonic circulation centres situated over the Mediterranean basin. Under these conditions, enhanced surface westerlies blowing from the Atlantic prevail in northern Europe. In contrast, the following five patterns (CT6, CT7, CT8, CT9 and CT10) represent typical cyclonic centres. CT6, an enhanced, deep low centre is located between the British Isles and the Scandinavia Peninsula, which appears in winter and affects the weather of northwestern Europe. CT7 presents a similarly strong, deep low-pressure centre to that in CT6, although in this case it is located east of the Baltic Sea. The remaining three patterns (CT8, CT9 and CT10) present typical cyclonic centres, located around the Mediterranean basin, and relate to areas of local cyclogenesis (Kostopoulou and Jones, 2007). The final three patterns (CT11, CT12 and CT13) are those occurring particularly during summer, representing basically the interaction of the Azores anticyclone with the summer Asian Thermal Low, which prevails throughout the eastern Mediterranean. One might notice that CT11 resembles CT9, however it must be noted that during CT9 the low-pressure centre over the easternmost Mediterranean is not related to the summer Asian Thermal Low (as in CT11). This Low is associated with frontal depressions that generate over secondary cyclogenesis areas in the Mediterranean, such as the Aegean Sea and Cyprus (Kostopoulou and Jones, 2007). It is further noted that CT12 and CT13 are considered subtypes of CT11, with a secondary centre of high/low pressure in eastern Europe.

The frequency of occurrence of each CT is calculated for the year of study (Fig. 6). CT11 is found to be the most frequent type (approx. 17% of the days), mainly observed during summer time. The cyclonic types CT7, CT6 also represent common circulation patterns (14 and 12%, respectively).

A qualitative evaluation of modelled CO concentrations at the three PC subregions is performed, both for S_2 and S_1 and in relation to the CTs, based on the standard statistics parameters. The calculated mean biases and mean errors (in percentage) of the two model configurations in relation to each CT are presented for PC1, PC2 and PC3 groups in Fig. 6.

As far as PC1 subregion is concerned, it is found that S_2 performs better than S_1 for the majority of patterns, with the best results obtained when CT2, CT3, CT6, CT10, CT11 and CT12 dominate this region. In particular, good results are obtained when the air flow reaches the PC1 domain from the west, as it drifts from across the Atlantic region (CT3 and CT11). Similarly, prevailing large-scale circulation associated with westerly wind bursts is observed during CT6. The nested-grid model has the best performance in comparison to the global model for CT12 (up to ∼22% improvement), which is one of the least frequent

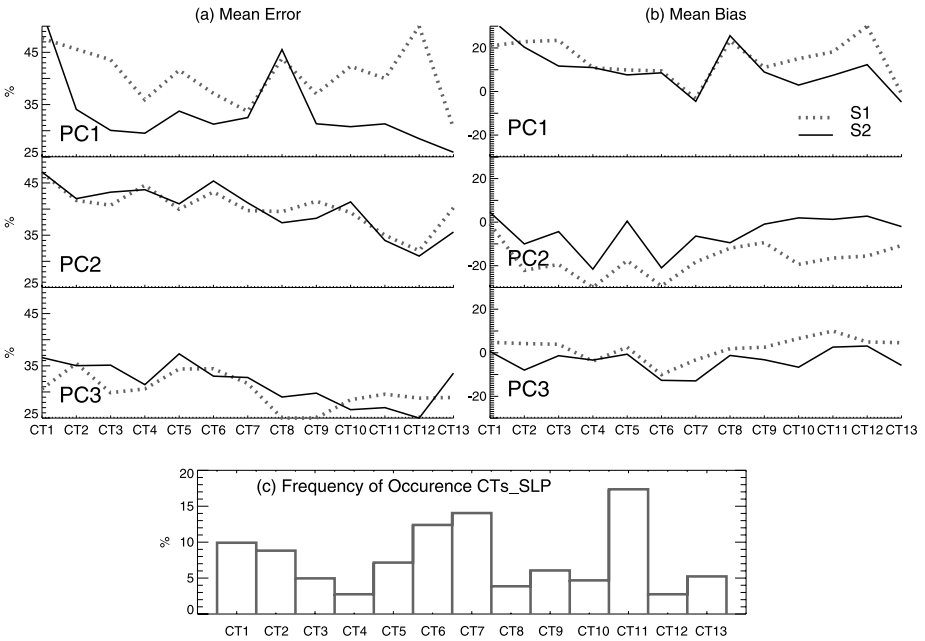

Fig. 6. Mean biases (MB) and mean errors (ME) calculated for S_1 and S_2 in relation to each of the 13 circulation types (CTs) at mean sea level, expressed in percentage (%) for the three principal components (PC1, PC2 and PC3). The frequency of occurrence of each CT for the year of study is also presented.

types within the year, as it is observed only a few times during summer. However, a similar, and more frequent, circulation is described by CT2, which is also better represented by the S_2 (up to ∼12% improvement). During these types, the occurrence of an anticyclone centre in eastern Europe, veers a southeasterly flow towards the PC1 domain. Southerly origin of airflow is also found in CT10. During this type, the cyclonic circulation associated with the low-pressure centre over the Adriatic Sea causes southwesterly airflow from southern Europe to intrude into the PC1 area. Results are also better for S_2, but to a lesser degree, for the majority of the rest CTs (C4, C5, C7, C9 and C13). In general, it is seen that the nested-grid model captures more successfully the pollutants distribution for stations in PC1 group when the local circulation is associated with western or southerly induced airflow. The good performance of this model configuration is attributed to the consideration of more detailed GEOS-3 meteorological data, enhanced spatial resolution in topography and higher advection and convection time-steps, which result in a more accurate representation of transport and mixing in S_2 than S_1. Consequently, the nested-grid model in most cases can resolve the synoptic circulation more precisely than the global model.

On the other hand, it is noted that a moderate performance, similar to that of the global model, is demonstrated by the nested-grid model when the PC1 subregion is under CT1 and CT8 conditions. During CT1, the anticyclone centre is situated right above the domain specified by PC1. In this case, the pressure gradient is weak across this region and without airflow intrusions from adjacent regions. During the CT8 pattern, a cell of low pressure is located in western Mediterranean and under these conditions, a weak pressure gradient and a weak airflow drifting from a northwestern or western direction are observed in the PC1 region. Hence, it may be concluded that S_2 does not seem to improve results significantly during stagnant circulation conditions, attributed to the fact that the mixing processes are similar in both models.

Overall, S_2 results are significantly improved under most CTs (up to ∼22% in case of CT12) for PC1 stations. As most of the stations belonging to this group are close to strong sources, differences between the CO concentrations calculated by S_1 and S_2 are also strongly attributable to the differences found between their anthropogenic CO emission densities. This appears more pronounced in stations at a short distance from the coast, attributed, as aforementioned in the previous section, to the lower emission rates in the coarse grids that include a large fraction of sea.

Good results are obtained for the region defined by PC2, too. In particular, lower biases are revealed for synoptic conditions represented by CT4, CT5, CT8, CT9, CT10 and CT13 patterns. More specifically, in all the cases that the nested-grid model substantially improves results in PC2 subregion, the major routes of airflow towards this area arrive from the west. Overall, S_2 results are significantly improved under most synoptic categories for the PC2 group (up to ∼17% for CT10). As the majority of these stations are located to a mountainous region, both models' results are largely influenced by topographical effects. However,

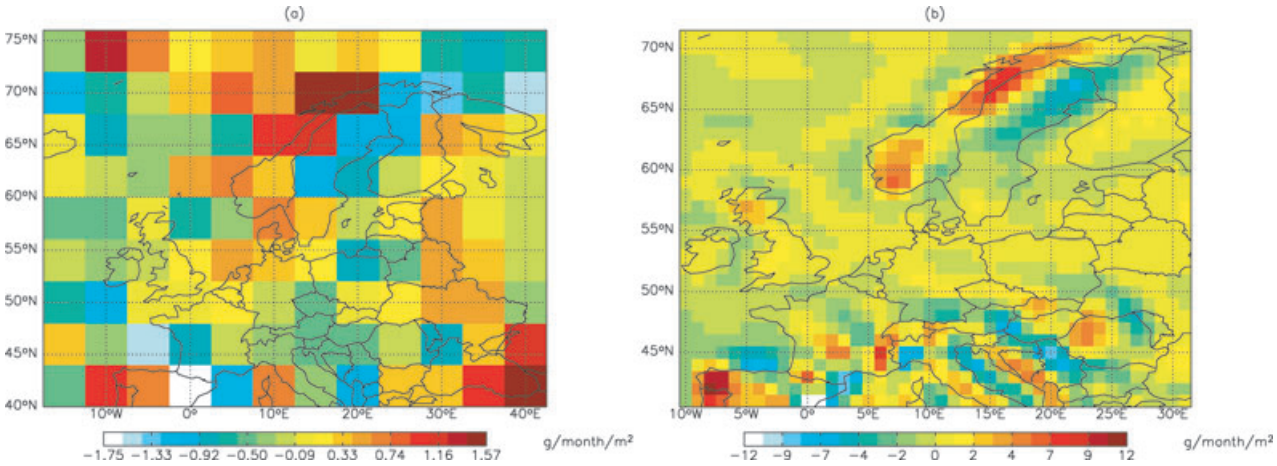

Fig. 7. Vertical fluxes at 850 hPa (∼2 km) in winter in Europe considered in (a) the global model and (b) the nested-grid model. Negative (positive) fluxes represent upward (downward) fluxes.

as mentioned in the previous section, S_2 improves performance in comparison to S_1 at stations of high altitude, which explains the nested-grid model's ability to simulate atmospheric conditions more accurately for PC2 group. Moreover, it is noted that although the stations belonging to PC2 subregion are remote from major sources, with lower emission rates in S_2 than in S_1, their mean annual concentrations are similar and particularly high for both runs. Consequently, the nested-grid simulation is able to account for strong pollution transport from neighbouring heavily polluted regions (e.g. Po-valley, northern Italy), resulting in high CO levels at these remote stations. Indeed, it becomes evident that the transported pollution is better represented in the nested-grid model than in the global model. In particular, strong upward fluxes in S_2 over the polluted areas favour the ventilation of the lower troposphere and the CO dilution, driving pollution to upper levels (Fig. 7b), where it is transported by the synoptic circulation towards the mountainous region. In this case, the strong downward fluxes in S_2 favour accumulation of CO at surface. On the other hand, the global model is unable to capture transport on scales smaller than 400–500 km and mixing is much slower (Fig. 7a), attributed to its coarse resolution.

Less satisfactory results are obtained for PC3 group, with S_2 improving results by up to ∼7% (for CT11). This was nevertheless not surprising, as this group includes stations situated far apart from each other, and therefore exhibit diverse characteristics. In such cases, the nested-grid model reveals poor performance skills under most of the prevailing synoptic-scale CTs, given the diversity of mesoscale flows observed in each site and the diversity in the other characteristics of the stations. Furthermore, the low spatial variability of emissions in this region is not capable of improving the calculated concentrations in the nesting application.

Similarly, spatial circulation patterns are analysed at the geopotential level of the 850 hPa (CT_{850}) (not shown). It is found that the nested-grid model simulates CO concentrations better than the global model for most of the CTs (Fig. 8). In contrast, S_2 shows poor simulation skills when a centre of high geopotential heights is situated above the domain of study. This is in accordance with the previous findings that revealed negligible improvement of the results when a high-pressure system at surface dominates the weather across western Europe (i.e. CT1).

4.3 Case studies

In this section, CO surface concentrations in Europe are studied during high pollution events. To this aim, CO is examined at one rural station in the Netherlands, where particularly enhanced concentrations in comparison to the background levels were observed during the cold period of 2001. CO is also studied during summer using data from a Greek rural station, in order to assess the strength of the model to reproduce high concentrations in a region that is under the influence of dominant summer-time synoptic features.

4.3.1 High CO pollution event in winter. In January 2001, recorded CO concentrations at Zegveld-Oude Meije (NL0229A), a rural background station located outside a built-up area (van Elzakker, 2001), were characterized by periodic rises and falls that lasted from a few hours to a few days (Fig. 9). Particularly, during 15–20 January, CO rapidly increased from rural concentrations to significantly higher levels for the following 3 days, with peak values (hourly concentrations of 800–1800 ppbv) especially apparent during the period 17–20 January.

The study of the surface synoptic patterns and the associated meteorological conditions reveals that low pressures (assigned to CT7) prevailed over the study area 4–5 d before the event (10–11 January). During this period, CO concentrations are substantially different between the two models, with the nested-grid simulation capturing the observed rises and falls, as opposed to a poorer performance of the global model. As already

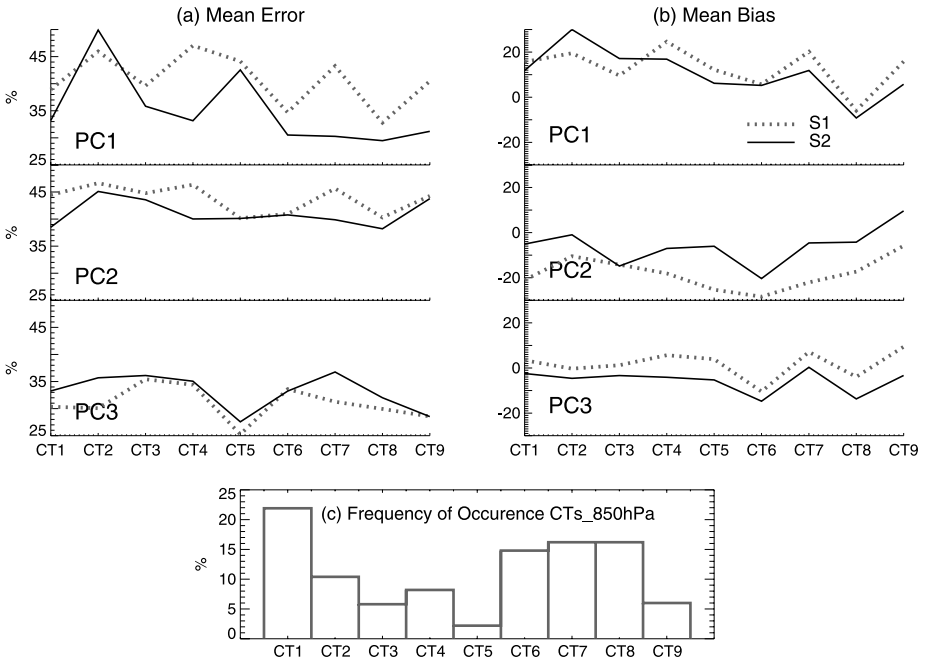

Fig. 8. As in Fig. 6, but for 9 circulation types at the geopotential level of the 850 hPa (CT_{850}).

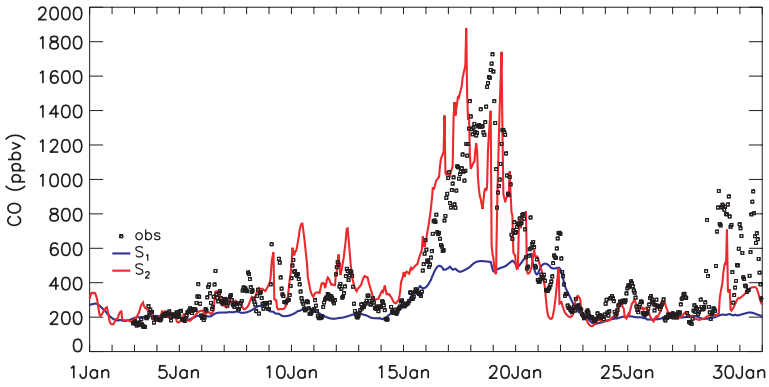

Fig. 9. Measured and modelled hourly CO concentrations at the rural background station Zegveld-Oude Meije (NL0229A) in the Netherlands during January 2001.

discussed, S_2 slightly improves results under these synoptic conditions. Therefore, simulated wind speed and wind direction in both modelling approaches do not differ much on those days (Figs 10a and b). However, temperature is significantly higher in S_1 (Fig. 10c), revealing that the global model fails to capture the passing cold front. Moreover, the enhanced mixing in the global model (Fig. 10d) favours the artificial CO dilution in the coarse grids, retaining CO in lower levels; thus differences between CO predictions and observations increase in this model configuration. The next couple of days (12–14 January), the low pressure systems were followed by large anticyclonic patterns (CT1), dominating over an extensive area of the western and central Europe, extending from the United Kingdom and the Netherlands to Poland and large part of Austria and Hungary. However, the observed CO concentrations at the examined station remained relatively low, since the prevailing weak wind flow did not favour significant pollution transport towards this area. It is worth noting that especially on 14–15 January (both assigned to CT1) the global model simulates CO levels closer to the observations than the nested-grid model. As aforementioned, both models' performance is limited under this circulation pattern due to the prevailing stagnant conditions and the associated limited mixing. Nevertheless, the higher wind speed in the global simulation dilutes more CO and decreases its levels, resulting in better agreement with the observed values.

From January 16 and onwards, an eastward shift of the system was observed, and the high-pressure centre was prominent over eastern Europe and parts of European Russia. Under this circulation (CT2), low southeasterly winds spiralled outward from the outskirts of the high-pressure centre towards the study region. Meanwhile, an anticyclone was found at 850 hPa and a low-pressure system at 500 hPa enhanced the high pressures in the lower troposphere. Particularly on January 16 and 17, the prevailing south–southeasterly winds of low intensity transferred

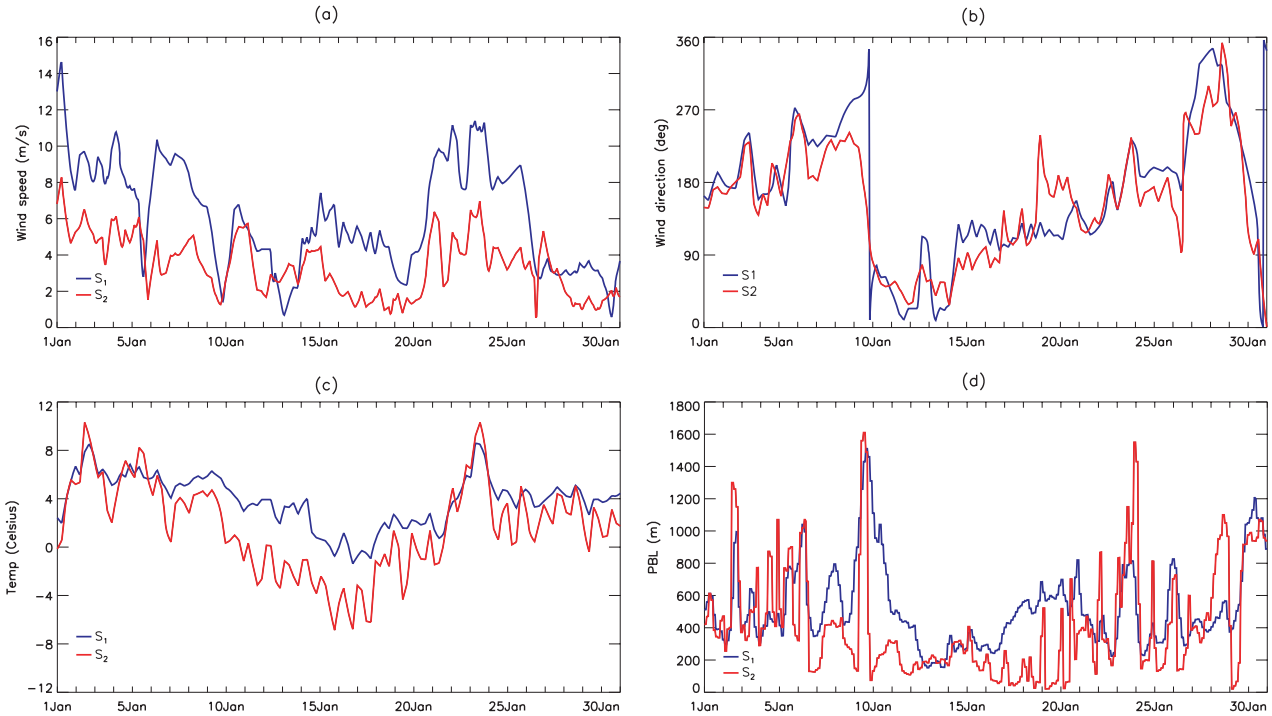

Fig. 10. Wind speed (a), wind direction (b), temperature (c) and PBL heights (d) calculated by GEOS-CHEM model nested-grid (S_2) and global (S_1) simulations at the rural background station Zegveld-Oude Meije (NL0229A) in the Netherlands during January 2001. Measurements were not available.

polluted air masses from heavily polluted neighbouring areas. This transport is well simulated by S_2, resulting in the gradual increase of CO concentrations. The global model presents also a small increase in CO values. However, its limited performance under the CT2 type results in higher winds (and consequently in deep mixing heights), retaining CO in much lower levels. On January 18, a cyclonic circulation began to form west of the Netherlands, which, combined with the high pressure to the east, enhanced the southwesterly flow. S_2 captures this sharp change of wind direction successfully but with a time lag of few hours, while S_1 winds retain the southeasterly flow. This weak low-pressure system, centred to the west of the station, was well developed on the 19th of January. The shallow mixing heights prevented pollutants dilution, trapping them close to surface under the influence of the prevailing low synoptic winds. From Fig. 9, it is evident that this pollution event is successfully captured by the fine model. On the other hand, the enhanced mixing and the high wind speeds in the global model retain CO in lower levels. The limited representation of meteorological patterns and transport processes in the $4^\circ \times 5^\circ$ grids becomes also evident from the GEOS-3 meteorological patterns (not shown).

From January 20 and onwards, the low pressure moved further east and CO levels began to decline, as a warm front, followed by increase in temperature and wind intensity, forced the high CO concentrations to dilute. Once more, CO levels and daily variability calculated by S_2 are in good agreement with measurements, owing to this model's ability to capture the assigned CTs and the associated wind regimes. Overall, the nested-grid model has a very good performance during the high pollution event (MO = 843.3 ppbv, $MB_{S2} = 47.9$ ppbv and $ME_{S2} = 274.8$ ppbv), significantly more accurate (up to 42%) than the global model ($MB_{S1} = -400.7$ ppbv, $ME_{S1} = 404.8$ ppbv).

4.3.2 High CO pollution event in summer. In summer, a strong east–west surface pressure difference is generated between the Azores high and the Asian monsoon low-pressure patterns, which cause northerly flow in the lower troposphere over the Eastern Mediterranean, particularly in August (e.g. Tombrou et al., 2009). Indeed, the examination of the synoptic patterns during August 2001 reveals that the prevailing conditions over the Greek territory mainly corresponded to three synoptic categories (CT11, CT12 and CT13), being associated with strong northerlies over the Aegean Sea. The air flow pattern at the upper level of 850 hPa also originated mainly from the northern sector (N–NE) along the Aegean Sea (assigned mainly to types $CT1_{850}$ and $CT7_{850}$), which turned to NW over the Greek Island of Crete.

In order to study long range transport towards this area, CO measurements were collected at Finokalia (Fig. 11), a rural coastal station (130 m above sea level) on the northeastern part of Crete (35°19′N, 25°40′E, Fig. 3), during 1–16 August 2001, in the framework of MINOS campaign (Lelieveld et al., 2002a). Under the prevailing conditions, pollution transport was

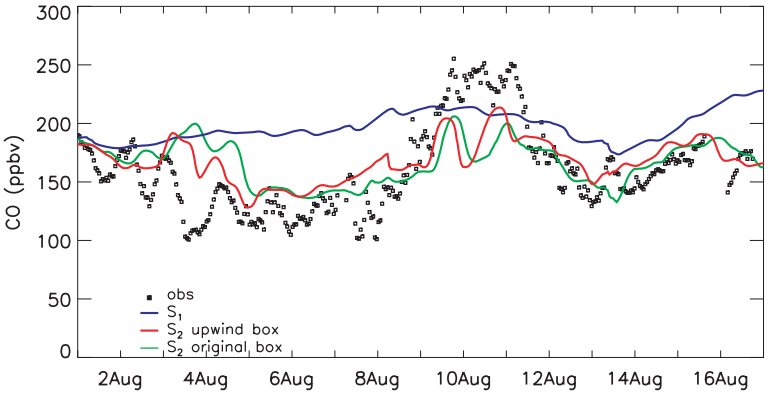

Fig. 11. Measured and modelled hourly CO concentrations at the rural background station Finokalia in Greece, during 1–16 August in 2001 of the MINOS campaign (Lelieveld et al., 2002a; Salisbury et al., 2003).

favoured along the northwestern Turkish coast and the north-eastern boundary of Greece, most likely from the Sea of Azov in NE Europe where significant CO production was evident due to a large number of fires (Salisbury et al., 2003), resulting in significant increase of CO levels at Finokalia.

In order to investigate the performance of the two modelling applications during this pollution transport event (Fig. 11), results are examined in relation to synoptic circulations. During all types, the prevailing wind at Finokalia was of strong intensity (Fig. 12a), originating from the northwest (Fig. 12b). Hence, the nested-grid model results are also studied at the adjacent upwind grid to the original Finokalia's grid, on the northwesterly direction in the Aegean Sea. Modelled temperature (Fig. 12c) against measurements (e.g. Krol et al., 2005) and PBL heights (Fig. 12d) are also examined.

Measured CO concentrations at Finokalia (e.g. Salisbury et al., 2003) are reasonably well simulated by the nested-grid model. The best model-observation agreement is found during 5–8 and 11–16 of August, when the nested-grid model approach captures more successfully the measured CO levels in comparison to the overestimated values simulated by the global model. This is attributed to the better representation of the prevailing CT11 and CT13 by S_2 in comparison to S_1. The limited representation of the meteorological patterns and transport processes in the $4^\circ \times 5^\circ$ grids becomes also evident from the GEOS-3 meteorological patterns (not shown). Particularly, in most of the

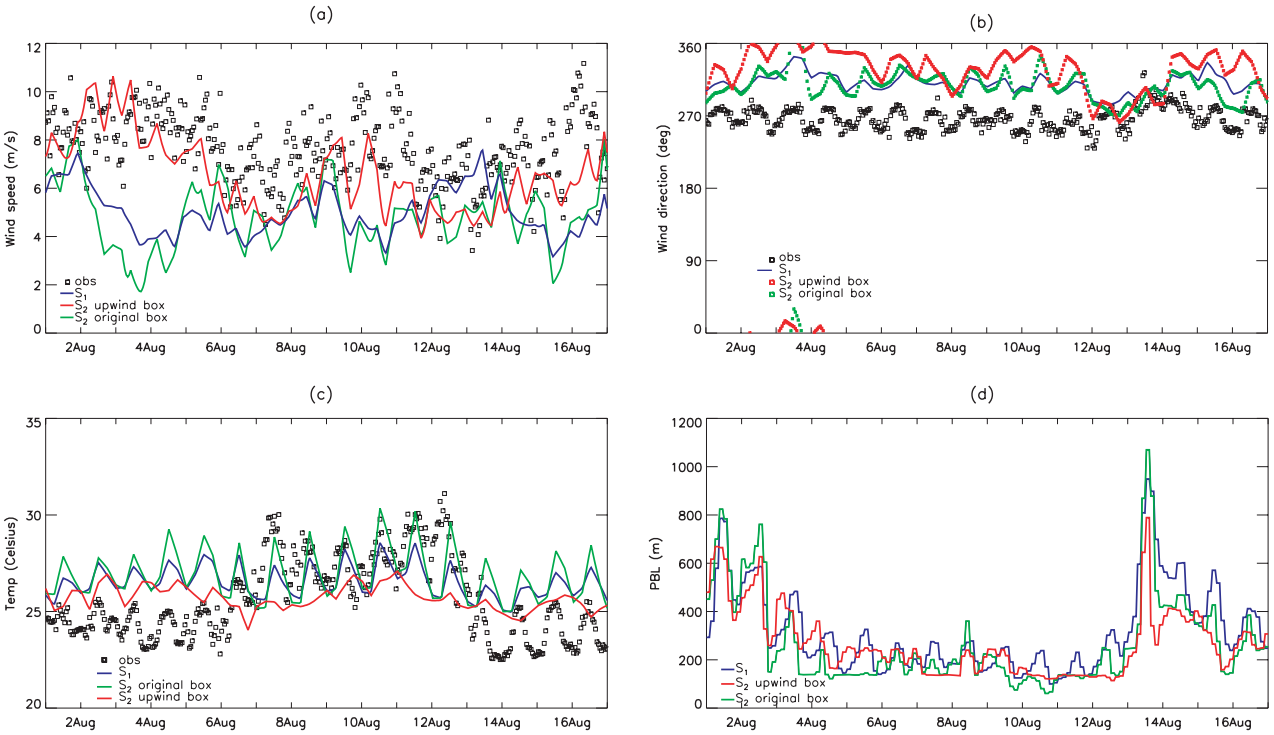

Fig. 12. Wind speed (a), wind direction (b), temperature (c) and PBL heights (d) calculated by GEOS-CHEM model nested-grid (S_2) and global (S_1) simulations at Finokalia during 1–16 August 2001. Measurements are plotted when available (MINOS, Lelieveld et al., 2002a; Krol et al., 2005).

days, the centres of the Lows and Highs are more precisely located in S_2 than in S_1, while the extension of the Asian Low over the Aegean is clearly deeper. Furthermore, the synoptic conditions that prevailed during this period at the 850 hPa ($CT1_{850}$, $CT7_{850}$) are better represented in S_2 than in S_1. The limited performance of the global model through the whole period is also attributed to the fact that the coarse grid including the Finokalia site aggregates emissions from the entire area of Crete.

Biases in the nested-grid model simulation are observed when the area is dominated by strongly variable atmospheric circulation (e.g. 3–4 and 9–10 August). Under these conditions, a distinct (i.e. well-organised) synoptic circulation fails to establish over the area in the model, resulting in a mismatch of the position of the low and high-pressure centres of GEOS-3 assimilated data in relation to the real atmospheric circulation. Overall, the nested-grid model simulation reproduces reasonably well the CO observations during the whole period (MO = 159.5 ppbv, MB_{S2} = 5.2 ppbv and ME_{S2} = 22.6 ppbv), significantly more accurately (up to ∼20%) than the global model, which reveals poorer performance (MB_{S1} = 36.4 ppbv, ME_{S1} = 43 ppbv).

5. Conclusions

The application of the nested-grid simulation of the global CTM GEOS-CHEM over the European domain demonstrated that this model configuration has a very good ability in capturing the seasonal signals and the levels of CO concentrations at rural background areas throughout the year. Based on extended statistical evaluation for 31 stations, it was found that the nesting model approach shows the lowest (largest) biases in warm (cold) periods, tracking CO in most cases more accurately than the global model, particularly (a) close to significant anthropogenic activity, (b) at high altitudes and (c) at short distance from the coast.

In order to determine the differences between the nested-grid configuration and the global GEOS-CHEM model, a rotated PCA was applied based on daily CO modelled concentrations in 2001, yielding three PCs that defined three subregions in the study domain. The first subregion (PC1) accumulated stations located in the northern and western part of the study region, close to the major anthropogenic sources, with significantly higher mean emission rates (up to ∼50%) and in general at low altitudes. The second subregion (PC2) included stations that were located in the southern part of the examined area, mainly at a long distance from major sources (with emissions at ∼1/2 of that considered in PC1) and at a mean altitude of ∼400 m. In the third subregion (PC3), stations were located in the eastern part of the examined area, with lower background emissions in comparison to the other two groups and at similar mean altitudes with PC2.

The CO concentrations for each of the three PCs groups were examined, in relation to the circulation patterns prevailing over Europe, at MSL and at the geopotential level of the 850 hPa. It was found that nested-grid model's results significantly improve for PC1 stations (up to ∼22%) and PC2 (up to ∼17%), while improvement is lower for PC3 (up to ∼7%). This model configuration presents better performance when the prevailing circulation patterns are associated with westerly flow, while poorer skills are found during stagnant conditions. Similar results are obtained for the CTs at 850 hPa. Moreover, it was found that transport and mixing processes are better represented by the nesting simulation than in the global run. This was particularly evident in high altitude regions, where the pollution advection and convection processes from highly polluted neighbouring areas are better captured by the nested-grid model.

Furthermore, it was seen that differences in CO concentrations over Europe between the two model configurations are related particularly to the hydroxyl radical behaviour. CO and OH concentrations depend, particularly at remote regions, not only on emissions and the background levels of their precursors, but on their transport as well.

In addition, the nested-grid model proves to reproduce the day-to-day variability of the CO concentrations at rural stations during high pollution events, both in the cold and the warm periods, as opposed to the poorer global model's performance. The improvement in the nesting modelling approach in comparison to the global model application in these cases reaches up to ∼40%.

Deviations of the nested-grid model from the observations were partially attributed to the uncertainty of the emission inventories, mismatches in the meteorological data representation, lack of vertical variation in the injection heights of the emissions from fires and the full-mixing PBL scheme considered in the model. Recently, the consideration of the non-local scheme formulated by Holtslag and Boville (1993) in the global model was found to improve vertical distribution of NO_2 and O_3 in the lower troposphere relative to results derived using the full-mixing assumption (Lin and McElroy, 2010), although the coarse resolution in the global model was a limiting factor (Lin et al., 2010). The grid size in the nested-grid model, although of higher resolution, still limited modelling skills in simulating small-scale weather systems, as well as emissions and model predictions at station-scales; hence the accuracy of the results is reduced. Moreover, smaller biases were attributed to the fact that some CO sources and sinks of lesser importance are not considered in the model.

6. Acknowledgments

This work was supported by the Greek General Secretariat for Research and Technology in the framework of a bilateral collaboration program between National Observatory of Athens (Greece) and Harvard University (U.S.A.), with leaders, respectively, Dr. C. Giannakopoulos and Professor D. J. Jacob. We would like to acknowledge Yuxuan X. Wang and Randal Martin for providing, respectively, the nested-grid set-up and the global $1^\circ \times 1^\circ$ data, Professor N. Michalopoulos and Dr. J. Sciare for the CO concentration measurements as well as the

acquisition of the meteorological data, collected in the framework of MINOS campaign (Lelieveld et al., 2002a) at Finokalia site and European Environmental Agency (© E.E.A, Copenhagen, 2001) for Airbase data. Grateful acknowledgments to Professor A.G. Russell for his fruitful comments and suggestions, Associate Professor D.K. Pissimanis for his assistance on the interpretation of the synoptic circulation patterns and Dr. S. Koumoutsaris for his support on modelling issues. Finally, we would like to thank the two anonymous reviewers for their constructive criticism and suggestions that have significantly contribute to the improvement of this manuscript.

References

Allen, D. J., Rood, R. B., Thompson, A. M. and Hudson, R. D. 1996a. Three dimensional radon222 calculations using assimilated data and a convective mixing algorithm. *J. Geophys. Res.* **101**(D3), 6871–6881.

Allen, D., Kasibhatla, P., Thompson, A., Rood, R., Doddridge, B. and co-authors. 1996b. Transport-induced interannual variability of carbon monoxide determined using a chemistry and transport model. *J. Geophys. Res.* **101**(D22), 28655–28669.

Auvray, M. and Bey, I. 2005. Long-range transport to Europe: Seasonal variations and implications for the European ozone budget. *J. Geophys. Res.* **110**, D11303, doi:10.1029/2004JD005503.

Benkovitz, C. M., Scholtz, M. T, Pacyna, J., Tarrason, L., Dignon, J. and co-authors. 1996. Global gridded inventories of anthropogenic emissions of sulfur and nitrogen. *J. Geophys. Res.* **101**, 29239–29253.

Bergamaschi, P., Frankenberg, C., Meirink, J. F., Krol, M., Dentener, F. and co-authors. 2007. Satellite chartography of atmospheric methane from SCIAMACHY on board ENVISAT: 2. Evaluation based on inverse model simulations. *J. Geophys. Res.* **112**, D02304, doi:10.1029/2006JD007268.

Berkvens, P. J. F., Botchev, M. A., Lioen, W. and Verwer, J. G. 1999. A zooming technique for wind transport of air pollution, Finite Volumes for Complex Applications II—Problems and Perspectives, Duisburg, Germany. pp. 499–506. Hermes. ISBN 2-7462-0057-0.

Bey, I., Jacob, D. J., Yantosca, R. M., Logan, J. A., Field, B. and co-authors. 2001. Global modeling of tropospheric chemistry with assimilated meteorology: model description and evaluation. *J. Geophys. Res.* **106**, 23073–23095, doi:10.1029/2001JD000807.

Chen, D., Wang, Y., McElroy, M. B., He, K., Yantosca, R. M. and co-authors. 2009. Regional CO pollution and export in China simulated by the high-resolution nested-grid GEOS-Chem model. *Atmos. Chem. Phys.* **9**, 3825–3839.

Crutzen, P. J. and Zimmermann, P. H. 1991. The changing photochemistry of the troposphere. *Tellus* **43AB**, 136–151.

Daniel, J. S. and Solomon, S. 1998. On the climate forcing of carbon monoxide. *J. Geophys. Res.* **103**, 13249–13260.

Derwent, R. G., Simmonds, P. G., Seuring, S. and Dimmer, C. 1998. Observation and interpretation of the seasonal cycles in the surface concentrations of ozone and carbon monoxide at Mace Head, Ireland from 1990 to 1994. *Atmos. Environ.* **32**(2), B145–157.

Duncan, B. N., Martin, R. V., Staudt, A. C., Yevich, R. M. and Logan, J. A. 2003. Interannual and seasonal variability of biomass burning emissions constrained by remote-sensed observations. *J. Geophys. Res.* **108**(D2), 4040, doi: 10.1029/2002JD002378.

Duncan, B. N. and Bey, I. 2004. A modelling study of the export pathways of pollution from Europe: seasonal and interannual variations (1987–1997). *J. Geophys. Res.* **109**, D08301, doi:1029/2003JD004079.

Duncan, B. N., Logan, J. A., Bey, I., Megretskaia, I. A., Yantosca, R. M. and co-authors. 2007. The global budget of CO, 1988–1997: source estimates and validation with a global model. *J. Geophys. Res.* **112**, D22301, doi:10.1029/2007JD008459.

Emeis, S. and Schafer, K. 2006. Remote sensing methods to investigate boundary-layer structures relevant to air pollution in cities. *Boundary Layer Meteorol.* **121**, 377–385.

Fiore, A. M., Horowitz, L. W., Purves, D. W., Levy II, H., Evans, M. J. and co-authors. 2005. Evaluating the contribution of changes in isoprene emissions to surface ozone trends over the eastern United States. *J. Geophys. Res.* **110**, D12303, doi:10.1029/2004JD005485.

Heald, C. L., Jacob, D. J., Fiore, A. M., Emmons, L. K., Gille, J. C. and co-authors. 2003. Asian outflow and transpacific transport of carbon monoxide and ozone pollution: an integrated satellite, aircraft and model perspective. *J. Geophys. Res.* **108**(D24), 4804, doi:10.1029/2003JD003507.

Holtslag, A. and Boville, B. 1993. Local versus nonlocal boundary-layer diffusion in a global climate model. *J. Climate* **6**, 1825–1842.

Intergovernmental Panel on Climate Change (IPCC). 2001. *The Scientific Basis Contribution of Working Group I to the Third Assessment Report of the Intergovernmental Panel on Climate Change* (eds J. T. Houghton, Y. Ding, D. J. Griggs, M. Noguer, P. J. van der Linden and D. Xiaosu). Cambridge University Press, UK, 944.

Jacob, D. J. 1999. *Introduction to Atmospheric Chemistry*. Princeton University Press, Princeton. ISBN 0-691-00185-5.

Jacob, D. J., Field, B. D., Jin, E., Bey, I., Li, Q. and co-authors. 2002. Atmospheric budget of acetone. *J. Geophys. Res.* **107**, D10, doi:10.1029/2001JD000694.

Jaeglé, L., Jaffe, D., Price, H. U., Weiss, P., Palmer, P. I. and co-authors. 2003. Sources and budgets for CO and ozone in the northeastern Pacific during the spring of 2001: results from the PHOBEA -II experiment. *J. Geophys. Res.* **108**, 8803, doi:10.1020/2002JD003121.

Jolliffe, I.T. 1993. Principal component analysis: a beginner's guide-II. Pitfalls, myths and extensions. *Weather* **48**, 246–253.

Kallos, G., Astitha, M., Katsafados, P. and Spyrou, C. 2007. Long-range transport of anthropogenically and naturally produced particulate matter in the Mediterranean and North Atlantic: current state of knowledge. *J. Appl. Met. Clim.* **46**(8), 1230–1251.

Kaminski, J. W., Neary, L., Struzewska, J., McConnell, J. C., Lupu, A. and co-authors. 2008. GEM-AQ, an on-line global multiscale chemical weather modelling system: model description and evaluation of gas phase chemistry processes. *Atmos. Chem. Phys.* **8**, 3255–3281.

Kanakidou, M., Dentener, F. J., Brasseur, G. P., Berntsen, T. K., Collins, W. J. and co-authors. 1999. 3D global simulations of tropospheric CO distributions: results of the GIM/IGAC intercomparison 1997 exercise. *Chemosphere Global Change Sci.* **1**, 263– 282.

Kanakidou, M. and Crutzen, P. J. 1999. The photochemical source of carbon monoxide: importance, uncertainties and feedbacks. *Chemosphere-Global Change Sci.* **1**, 91–109.

Kostopoulou, E. 2003. *The Relationships Between Atmospheric Circulation Patterns and Surface Climatic Elements in the Eastern Mediterranean*. Ph.D. thesis, University of East Anglia, Norwich.

Kostopoulou, E. and Jones, P. D. 2007. Comprehensive analysis of the climate variability in the eastern Mediterranean Part I: map-pattern classification. *Int. J. Climatol.* **27**, 1189–1214.

Krol, M., Houweling, S., Bregman, B., Van Den Broek, M., Segers, A. and co-authors. 2005. The two-way nested global chemistry-transport zoom model TM5: algorithm and applications. *Atmos. Chem. Phys.* **5**, 417–432.

Lelieveld, J., Berresheim, H., Bormann, S., Crutzen, P. J., Dentener, F. J. and co-authors. 2002a. Global air pollution crossroads over the Mediterranean. *Science* **298**, 794–799.

Lelieveld, J., Peters, W., Dentener, F. J. and Krol, M. C. 2002b. Stability of tropospheric hydroxyl chemistry. *J. Geophys. Res.* **107**(D23), 4715, doi:10.1029/2002JD002272.

Lelieveld, J., Dentener, F. J., Peters, W. and Krol, M. C. 2004. On the role of hydroxyl radicals in the self-cleansing capacity of the troposphere. *Atmos. Chem. Phys.* **4**, 2337–2344.

Li, Q., Jacob, D., Park, R., Wang, Y., Heald, C. and co-authors. 2005. North American pollution outflow and the trapping of convectively lifted pollution by upper-level anticyclone. *J. Geophys. Res.* **110**, D10301, doi:10.1029/2004JD005039.

Lin, S. J. and Rood, R. B. 1996. Multidimensional flux-form semi-Lagrangian transport schemes. *Mon. Wea. Rev.* **124**, 2046–2070.

Lin, J.-T., McElroy, M. B. and Boersma, K. F. 2010. Constraint of anthropogenic NO_x emissions in China from different sectors: a new methodology using multiple satellite retrievals. *Atmos. Chem. Phys.* **10**, 63–78.

Lin, J.-T. and McElroy, M. B. 2010. Impacts of boundary layer mixing on pollutant vertical profiles in the lower troposphere: implications to satellite remote sensing. *Atmos. Environ.* **44**, 1726–1739, doi: 10.1016/j.atmosenv.2010.02.009.

Liu, J., Drummond, J. R., Jones, D. B. A., Cao, Z., Bremer, H. and co-authors. 2006. *J. Geophys. Res.* **111**, D2, doi: 10.1029/2005JD006076.

Logan J. A., Prather, M. J., Wofsy, S. C. and McElroy, M. B. 1981. Tropospheric chemistry: a global perspective. *J. Geophys. Res.* **86**, 7210–7254.

Martin, R. V., Jacob, D. J., Yantosca, R. M., Chin, M. and Ginoux, P. 2003. Global and regional decreases in tropospheric oxidants from photochemical effects of aerosols. *J. Geophys. Res.* **108**, 4097, doi:10.1029/2002JD002622.

McLinden, C. A., Olsen, S., Hannegan, B., Wild, O., Prather, M. J. and co-authors. 2000. Stratospheric ozone in 3-D models: a simple chemistry and the cross-tropopause flux. *J. Geophys. Res.* **105**(D11), 14653–14665.

Min, J. Y., Paek, D., Cho S. I. and Min K. B. 2009. Exposure to environmental carbon monoxide may have a greater negative effect on cardiac autonomic function in people with metabolic syndrome. *Sci. Total Environ.* **407**(17), 4807–4811, doi:10.1016/j.scitotenv.2009.05.028.

Novelli, P., Steele, L. and Tans, P. 1992. Mixing ratios of carbon monoxide in the troposphere. *J. Geophys. Res.* **97**(D18), 20731–20750.

Novelli, P. C., Masarie, K. A. and Lang, P. M. 1998a. Distributions and recent changes of carbon monoxide in the lower troposphere. *J. Geophys. Res.* **103**(D15), 19015–19034, doi:10.1029/98JD01366.

Novelli, P. C., Connors, V. S., Reichle, H. G., Anderson, B. E., Brenninkmeijer, C. A. M. and co-authors. 1998b. An internally consistent set of globally distributed atmospheric carbon monoxide mixing ratios developed using results from an intercomparison of measurements. *J. Geophys. Res.* **103**(D15), 19285–19294.

Park, R. J., Jacob, D. J., Chin, M. and Martin, R. V. 2003. Sources of carbonaceous aerosols over the United States and implications for natural visibility. *J. Geophys. Res.* **108**(D12), 4355, doi:10.1029/2002JD003190.

Park, R. J., Jacob, D. J., Field, B. D., Yantosca, R. M. and Chin M. 2004. Natural and transboundary pollution influences on sulfate-nitrate-ammonium aerosols in the United States: implications for policy. *J. Geophys. Res.* **109**, D15204, doi:10.1029/2003JD004473.

Park, R., Jacob, D., Kumar, N. and Yantosca, R. 2006. Regional visibility statistics in the United States: natural and transboundary pollution influences, and implications for the Regional Haze Rule. *Atmos. Environ.* **40**(28), 5405–5423.

Parrish, D. D., Trainer, M., Buhr, M. P., Watkins, B. A. and Fehsenfeld, F. C. 1991. Carbon monoxide concentrations and their relation to concentrations of total reactive oxidized nitrogen at two rural U.S. sites. *J. Geophys. Res.* **96**(D5), 9309–9320.

Parrish, D. D., Holloway, J. S. and Fehsenfeld, F. C. 1994. Routine, continuous measurement of carbon monoxide with parts per billion precision. *Environ. Sci. Tecnol.* **28**, 1615–1618.

Pfister, G., Pétron, G., Emmons, L. K., Gille, J. C., Edwards, D. P. and co-authors. 2004. Evaluation of CO simulations and the analysis of the CO budget for Europe. *J. Geophys. Res.* **109**, D19304, doi:10.1029/2004JD004691.

Piccot, S., Watson, J. and Jones, J. 1992. A global inventory of volatile organic compound emissions from anthropogenic sources. *J. Geophys. Res.* **97**(D9), 9897–9912.

Price, C. and Rind, D. 1992. A Simple lightning parameterization for calculating global lightning distributions. *J. Geophys. Res.* **97**(D9), 9919–9933, doi:10.1029/92JD00719.

Raub, J. A., Mathieu-Nolf, M., Hampson, N. B. and Thom, S. R. 2000. Carbon monoxide poisoning – a public health perspective. *Toxicology* **145**(1), 1–14, ISSN 0300-483X, doi:10.1016/S0300-483X(99)00217-6.

Raub, J. A. 1999. Health effects of exposure to ambient carbon monoxide. *Chemosphere – Global Change Science* **1**(1–3), 331–351, ISSN 1465–9972, doi:10.1016/S1465-9972(99)00005-7.

Ravishankara, A. R., Dunlea, E. J., Blitz, M. A., Dillon, T. J., Heard, D. E. and co-authors. 2002. Redetermination of the rate coefficient for the reaction of $O(^1D)$ with N_2. *Geophys. Res. Lett.* **29**(15), 1745, doi: 10.1029/2002GL014850.

Salisbury, G., Williams, J., Holzinger, R., Lange, L., Xu, X. and co-authors. 2003. Ground-based PTR-MS measurements of reactive organic compounds during the MINOS campaign in Crete, July-August 2001. *Atmos. Chem. Phys.* **3**, 925–940.

Seinfeld, J. H. and Pandis, S. N. 2006. *Atmospheric Chemistry and Physics: From Air Pollution to Climate Change*, 2nd Edition. J. Wiley, New York.

Tombrou, M., Bossioli, E., Protonotariou, A. P., Flocas, H., Giannakopoulos, C., and Dandou, A. 2009. Coupling GEOS-CHEM with A Regional Air Pollution Model for Greece. *Atmos. Environ.* **43**(31), 4793–4804, ISSN 1352-2310, doi:10.1016/j.atmosenv.2009.04.003.

van Elzakker, B. G. 2001. Monitoring activities in the Dutch National Air Quality Monitoring Network in 2000 and 2001. *RIVM Report 723101 055*, National Institute of Public Health and the Environment RIVM, Bilthoven, The Netherlands.

Wang, Y., Jacob, D. J. and Logan, J. A. 1998. Global simulation of tropospheric O3-NOx-hydrocarbon chemistry 1. Model formulation. *J. Geophys. Res.* **103**(D9), 10713–10726, doi:10.1029/98JD00158.

Wang, Y. X., McElroy, M. B., Jacob D. J. and Yantosca, R. M. 2004a. A nested-grid formulation for chemical transport over Asia: applications to CO. *J. Geophys. Res.* **109**, D22307, doi:10.1029/2004JD005237.

Wang, Y. X., McElroy, M. B., Wang T. and Palmer, P. I. 2004b. Asian emissions of CO and NOx : constraints from aircraft and Chinese station data. *J. Geophys. Res.* **109**, D24304, doi:10.1029/2004JD005250.

Wang, H., Jacob, D. J., Le Sager, P., Streets, D. G., Park, R. J. and co-authors. 2009a. Surface ozone background in the United States: Canadian and Mexican pollution influences. *Atmos. Environ.* **43**(6), 1310–1319, ISSN 1352-2310, doi:10.1016/j.atmosenv.2008.11.036.

Wang, Y., Hao, J., McElroy, M. B., Munger, J. W., Ma, H. and co-authors. 2009b. Ozone air quality during the 2008 Beijing Olympics: effectiveness of emission restrictions. *Atmos. Chem. Phys.* **9**, 5237–525.

Wilks, D. S. 1995. *Statistical Methods in the Atmospheric Sciences: An Introduction*. Academic Press, San Diego, California, 467 pp.

Yevich, R. and Logan, J. A. 2003. An assessment of biofuel use and burning of agricultural waste in the developing world, Global Biogeochem. *Cycles* **17**(4), 1095, doi:10.1029/2002GB001952.

Supporting Information

Additional supporting information may be found in the online version of this article:

Appendix S1. Mean monthly surface concentrations of CO in Europe produced by the nested-grid simulation (S_2) in (a) winter and (b) summer.

Percentage difference between the predicted CO concentrations (C) calculated by the nested-grid (S_2) and the global (S_1) simulations of GEOS-CHEM $\{[(C_{S2}\text{-}C_{S1})/C_{S1}]\times 100\%\}$ for winter (c) and summer (d).

(a) Modelled OH distribution by the nested-grid (S_2) simulation of GEOS-CHEM in summer, (b) percentage difference of OH in summer calculated between the concentrations (C) calculated by the nested-grid (S_2) and the global (S_1) simulations of GEOS-CHEM, given by $[(C_{S2}\text{-}C_{S1})/C_{S1}] \times 100\%$.

Percentage difference of O_3 concentrations in summer at surface in Europe between the nested-grid (S_2) and the global (S_1) simulations of GEOS-CHEM predicted concentrations (C), given by $[(C_{S2}\text{-}C_{S1})/C_{S1}] \times 100\%$.

Appendix S2. Measured (Air Quality Database of the European Environmental Agency, http://www.eea.europa.eu/data-and-maps/data/airbase-the-european-air-quality-database-1) and modelled mean daily CO concentrations (in ppbv) calculated by the nested-grid (S_2) and the global (S_1) simulations of GEOS-CHEM for 31 stations in Europe in 2001.

Appendix S3. Statistical parameters equations.

Appendix S4. Composites of 13 circulation patterns at mean sea level over Europe based on the classification developed by Kostopoulou and Jones (2007).

Please note: Wiley-Blackwell is not responsible for the content or functionality of any supporting materials supplied by the authors. Any queries (other than missing material) should be directed to the corresponding author for the article.